Plasma Physics and Controlled Fusion

PAPER

Simulations of edge and scrape off layer turbulence in mega ampere spherical tokamak plasmas

To cite this article: F Militello *et al* 2012 *Plasma Phys. Control. Fusion* **54** 095011

View the article online for updates and enhancements.

Related content

- Numerical scalings of the decay lengths in the scrape-off layer
F Militello, V Naulin and A H Nielsen
- Experimental and numerical characterization of the turbulence in the scrape-off layer of MAST
F Militello, P Tamain, W Fundamenski et al.
- Dissipative processes in SOL turbulence
W. Fundamenski, O.E. Garcia, V. Naulin et al.

Recent citations

- Three-dimensional simulations of plasma turbulence in the RFX-mod scrape-off layer and comparison with experimental measurements
Fabio Riva *et al*
- Intermittent electron density and temperature fluctuations and associated fluxes in the Alcator C-Mod scrape-off layer
R Kube *et al*
- Impact of the plasma geometry on divertor power exhaust: experimental evidence from TCV and simulations with SolEdge2D and TOKAM3X
A Gallo *et al*

IOP ebooks™

Bringing you innovative digital publishing with leading voices to create your essential collection of books in STEM research.

Start exploring the collection - download the first chapter of every title for free.

This content was downloaded from IP address 194.81.223.66 on 21/09/2018 at 13:04

Plasma Phys. Control. Fusion **54** (2012) 095011 (10pp) doi:10.1088/0741-3335/54/9/095011

Simulations of edge and scrape off layer turbulence in mega ampere spherical tokamak plasmas

F Militello[1], W Fundamenski[1], V Naulin[2] and A H Nielsen[2]

[1] EURATOM/CCFE Fusion Association Culham Science Centre, Abingdon, Oxon, OX14 3DB, UK
[2] Association EURATOM-Risoe National Laboratory, OPL-128 Risoe, DK-4000 Roskilde, Denmark

Received 1 March 2012, in final form 11 June 2012
Published 1 August 2012
Online at stacks.iop.org/PPCF/54/095011

Abstract
The L-mode interchange turbulence in the edge and scrape-off-layer (SOL) of the tight aspect ratio tokamak MAST is investigated numerically. The dynamics of the boundary plasma are studied using the 2D drift-fluid code ESEL, which has previously shown good agreement with large aspect ratio machines. In this context, a MAST-TCV comparison is presented in order to link the present analysis to well documented references. Next, scans of various edge parameters, such as density, temperature and current, are performed in the simulations with the aim of characterizing the profiles, fluctuation level and statistics of the edge/SOL density and temperature. In addition, we also discuss how the system changes when the length of the divertor leg is modified. This allows one to better understand the regime of operation of the Super-X divertor which will be implemented on MAST-Upgrade. The results obtained qualitatively agree with experimental observations. In particular, a universal behaviour of the fluctuation statistics is found for disparate edge conditions. Furthermore, the density and temperature decay lengths are inversely proportional to the plasma current and the edge temperature, while they are rather insensitive to the edge density (not to be confused with the line-averaged density).

(Some figures may appear in colour only in the online journal)

1. Introduction

Understanding the mechanisms behind the particle and heat exhaust in magnetically confined plasmas is crucial in the perspective of achieving a viable operating regime for a reactor [1]. In particular, it is still unclear how the relevant scrape-off layer (SOL) features, such as its density and temperature e-folding length, scale with engineering and dimensionless parameters. These upstream SOL characteristics translate into heat and particle deposition patterns at the target and at the first wall, and eventually into material erosion and re-deposition patterns. Since for the next generation tokamaks the heat loads at the target will determine the achievable plasma performances in the core, the investigation of the exhaust physics has become a central problem in the fusion community.

While it was long recognized that the perpendicular transport, determining the plasma profile in the SOL, is caused by turbulence [2, 3], only recently it was experimentally accepted [4–18] and theoretically understood [19–22] that its nature is non-local, non-Gaussian and that it is dominated by the dynamics of coherent structures known as blobs (or filaments). The interpretation of the experimental observations within the framework of this rather exotic physics (as compared with standard core turbulence) produced excellent results. In particular, numerical simulations that capture the blob dynamics were able to faithfully reproduce experimental data on TCV [17, 18, 23, 24] and, partially, on JET [25].

Much of the emphasis, so far, was given to the ability of the codes to match single experimental observation, a required step in order to validate the codes themselves and the physical models they used. An alternative approach, which we use in this work, is to explore the operationally achievable parameter space of a machine and to determine how the SOL responds to variations of the edge parameters (e.g. density, temperature and current). The latter can only be obtained by modifying

 © 2012 IOP Publishing Ltd Printed in the UK & the USA

the engineering controlled quantities such as fuelling, input power and plasma current. It is important to note that in the experimental environment it is challenging to unambiguously determine the relation between the SOL features and certain edge parameters. Indeed, these can be modified only through scans in the engineering quantities, which simultaneously affect more than one edge parameter (e.g. during density scans it is not uncommon to have an effect on both the edge density and temperature, see [5, 7, 14, 26, 27]). The benefit of our numerical approach is that, within the theoretical model used, it allows one to single out the effect of a certain edge parameter *while keeping all the others fixed*. This allows to draw a clearer picture of the main players in the SOL dynamics.

The plasma configurations that we investigate are characteristic of the mega ampere spherical tokamak (MAST) which has previously provided interesting experimental observations of the evolution of the filamentary structures in the SOL [28, 29] and of SOL features in L-mode [16, 30]. This machine is characterized by a tight aspect ratio, which increases the curvature of the magnetic field and enhances the drive of the coherent turbulent structures (believed to be governed by an interchange mechanism in the SOL [20, 22]). In addition, the particular magnetic geometry of the machine is such that the safety factor at the edge of the plasma is relatively large (i.e. $q \approx 5$–10), thus enhancing the neoclassical Pfirsch–Shlüter transport coefficients.

Finally, it is worth mentioning that a new divertor with Super-X geometry [31] will be installed in the next upgrade of this machine, thus allowing a number of benefits for the plasma exhaust process. In particular, the longer connection length increases the SOL collisionality, which in turn leads to larger parallel temperature gradients in the background plasma and a colder environment at the target. Furthermore, the shift of the divertor plates towards larger major radii generates a wider wetted area (which scales with R), so that the heat loads will be more evenly distributed (a crucial problem in the spherical tokamak geometry). Our calculations provide a first attempt at predicting what is the impact of a longer connection length on the SOL turbulence and therefore at understanding the operating configuration of a Super-X divertor.

The paper is structured as follows. In section 2 we briefly present the model equations used in our simulations and we provide an overview of the physics they describe. Section 3 is devoted to the discussion of the numerical results obtained. Starting from a description of the numerical set-up, we then show a comparison between TCV and MAST, we comment on the effect of edge temperature, density and plasma current variations on the SOL features and finally we discuss how a longer divertor leg (reflecting the Super-X geometry) affects the average profiles and the fluctuation statistics in the boundary region of the plasma. Conclusions will be drawn in section 4.

2. Model and physical background

The mathematical model that we solve numerically [21] is well suited to represent the interchange dynamics that regulate the motion of the plasma blobs. We use a set of reduced drift-fluid equations, which describe the evolution of three scalar fields: the particle density (equal for ions and electrons, due to quasi-neutrality), n, the electron temperature, T, and finally the vorticity of the $\boldsymbol{E} \times \boldsymbol{B}$ motion, Ω, which is simply the Laplacian of the electrostatic potential.

The model assumes that the ion dynamics are not relevant (justified under collisional conditions [25]), an electrostatic response and it is two dimensional. Electromagnetic effects are neglected for the sake of simplicity, although they are likely to play a role in the SOL [32, 33]. The equations describe the evolution of the scalar quantities in the drift plane (i.e. the plane perpendicular to the magnetic field), while the dynamics in the parallel direction is modelled using parallel loss terms. In this sense, it is useful to remark that the model is not assuming an average in the parallel direction (which would cancel the third coordinate, but make the treatment of the advective operators quite complicated). The final assumption pertains to the geometrical location of the numerical box, which is assumed to represent only a region of the plasma in the outer mid-plane of the machine (this allows some geometrical factors to be simplified). A local slab approximation is therefore used and some toroidal curvature effects are lost.

The equations are dimensionless by virtue of a Bohm normalization. This means that the length scales are normalized to the hybrid Larmor radius (i.e. the ion Larmor radius calculated with the electron temperature, T), $\rho_s \equiv c_s/\Omega_i$, where $c_s \equiv \sqrt{T/m_i}$ and $\Omega_i \equiv ZeB/m_i$ is the ion gyro-frequency (m_i and Z are the ion mass and charge state, e is the electron charge and B the modulus of the confining magnetic field). The time scale is normalized to the inverse of the ion gyro-frequency, so that the diffusion coefficients are normalized to the Bohm diffusion, $\rho_s^2\Omega_i$.

The equations are

$$\frac{\partial n}{\partial t} + \frac{1}{B}[\phi, n] = nC(\phi) - C(nT_e) + D\nabla_\perp^2 n - \Sigma_n n, \tag{1}$$

$$\frac{\partial T}{\partial t} + \frac{1}{B}[\phi, T] = \frac{2}{3}TC(\phi) - \frac{7}{3}TC(T) - \frac{2}{3}\frac{T^2}{n}C(n) + \chi\nabla_\perp^2 T - \Sigma_T T, \tag{2}$$

$$\frac{\partial \Omega}{\partial t} + \frac{1}{B}[\phi, \Omega] = -C(nT_e) + \mu\nabla_\perp^2\Omega - \Sigma_\Omega\Omega, \tag{3}$$

$$\Omega = \nabla_\perp^2\phi. \tag{4}$$

Here, the Poisson bracket notation $B^{-1}[\phi, f] \equiv B^{-1}\boldsymbol{b} \times \nabla\phi \cdot \nabla f$ is used to represent the advection of the fields due to the $\boldsymbol{E} \times \boldsymbol{B}$ drift (f here is a generic scalar field). The curvature operator, due to the change of B in space, is given by $C(f) \equiv (\rho_s/R)\partial f/\partial y$, where R is the major radius and y is the 'poloidal' coordinate in the drift plane. The magnetic field, B, is assumed to vary as the inverse of the major radius, so that in the local slab approximation $B^{-1} \approx 1 + \epsilon + (\rho_s/R)x$, where ϵ is the inverse aspect ratio and x is the 'radial' coordinate (remember that we are limiting our calculation to the outer mid-plane).

On the right-hand side of equations (1)–(3), D, χ and μ are the normalized neoclassical collisional dissipative coefficients and represent the particle diffusion, the heat conductivity and

the viscosity, respectively (see [25] for their derivation):

$$D = (1 + 1.3q^2)(1 + \theta)\frac{\rho_e^2 \nu_{ei}}{\rho_s^2 \Omega_i} \tag{5}$$

$$\chi = (1 + 1.6q^2)\left[4.66\frac{\rho_e^2 \nu_{ee}}{\rho_s^2 \Omega_i} + \Theta_{ie} 2\frac{\rho_i^2 \nu_{ii}}{\rho_s^2 \Omega_i}\right] \tag{6}$$

$$\mu = (1 + 1.6q^2)\frac{3}{4}\frac{\rho_i^2 \nu_{ii}}{\rho_s^2 \Omega_i}. \tag{7}$$

In these expressions, ρ_e is the electron Larmor radius, $\nu_{ss'}$ is the collision frequency between the species s and the species s' (with 'i' for the ions and 'e' for the electrons), $\theta = T_i/T_e$ and $\Theta_{ie} \equiv [1 + (\nu^*_{e,\epsilon}/\nu^*_e)^2]^{-1}$ with the equipartition collisionality $\nu^*_{e,\epsilon} \approx 63$ for a deuterium plasma and the collisionality $\nu^*_e \equiv L_\parallel/\lambda_e$ ($L_\parallel$ is the mid-plane to target connection length and λ_e is the electron collisional mean free path). Note that q is the safety factor and the brackets that contain it represent the neoclassical correction to the dissipation coefficients.

Finally, Σ_n, Σ_T and Σ_Ω model the parallel losses of density, temperature and vorticity as the plasma blob expands in the direction of the magnetic field towards the divertor plates. These terms can be represented as the inverse of the characteristic loss times and are simply defined as [25]

$$\Sigma_n = \Sigma_\Omega = \frac{M_\parallel \xi c_s}{L_\parallel \Omega_i} \tag{8}$$

$$\Sigma_T = \frac{2}{3}\frac{\chi_{\parallel,e}}{L_\parallel^2 \Omega_i}, \tag{9}$$

where $M_\parallel$ is the Mach number of the parallel flows (assumed to be equal to 0.5 in all our simulations, see [25]), $\xi \equiv \sqrt{Z + \theta}$ and $\chi_{\parallel,e} = 3.2 v_{te}^2/\nu_{ee}(1 + 4/\nu^*_e)^{-1}$ is the parallel electron heat conduction, which includes a flux limiter correction for low collisionalities (v_{te} is the electron thermal velocity). The physical meaning of equations (8) and (9) is that along the magnetic field the particles and the perpendicular momentum are removed only through sub-sonic advection, while the heat is lost through heat conduction (which dominates over the advective loss when the electron collisionality is low to moderate). The Σ parameters are set to zero in the region of the plasma inside the last closed flux surface (i.e. the edge), while they take a finite value in the SOL. In addition, we assume that their value is increased by a factor 20 in the wall shadow region, which is only present in our simulations of TCV (see below).

In the presence of gradients of the thermodynamic quantities, equations (1)–(3) can generate interchange instabilities, which in turn produce turbulence in the edge region. Once the turbulent fluctuations cross the last closed flux surface, they self-propel in the SOL region due to the generation of a dipolar vorticity field. In other words, the magnetic drifts of the particles in an inhomogeneous magnetic field induce an electrical charge imbalance in the blob structure and hence a polarization in the 'poloidal' direction. This electric field produces a radial motion of the blob through this self-generated $\boldsymbol{E} \times \boldsymbol{B}$ drift [20, 22]. As the blob penetrates deeper into the SOL the parallel losses contribute to reduce its size and the amplitude of the perturbation, until it finally dissipates at the divertor plates or at the first wall, releasing its density and temperature excess on the material surfaces.

Before concluding this section, it is useful to briefly discuss some mathematical properties of the system of equations we are solving. The normalized equations contain only a limited number of free parameters, and once those are chosen the solution is completely defined (assuming, of course, that the boundary conditions are fixed as well, which is the case in all our simulations, see below). These parameters are D, χ, μ, $\Sigma_n = \Sigma_\Omega$, Σ_T, ρ_s/R and ϵ. From equations (5)–(9), their explicit dependence on the edge parameters is the following:

$$D \sim \chi \sim \mu \sim \frac{q^2 n_0}{B_0 T_0^{3/2}} \tag{10}$$

$$\Sigma_n = \Sigma_\Omega \sim \frac{T_0^{1/2}}{L_\parallel B_0} \tag{11}$$

$$\Sigma_T \sim \frac{T_0^{1/2}}{(4 + \nu^*_e) L_\parallel B_0} \tag{12}$$

$$\rho_s/R \sim \frac{T_0^{1/2}}{B_0 R_0}, \tag{13}$$

where the symbol $\sim$ means 'approximatively proportional to' and we have assumed $\theta \approx 1$ and $\Theta_{ie} \ll 1$, which is acceptable for the regime investigated. The latter assumption is required to write equation (10) which implies that the dissipative parameters are proportional to each other so that, in principle, only one is representative of all three. This is hardly surprising, since they are all representative of fluid collisional dissipation. Equation (12) shows that Σ_T scales differently with the edge parameters depending on the collisionality regime (this is due to the fact that at low collisionality the flux limiter correction becomes important). We therefore find that once the boundary conditions are fixed, the dynamics of the system are determined exclusively by four dimensionless plasma parameters (D, Σ_n, Σ_T and ρ_s/R) plus a geometrical one (ϵ, which however plays a smaller role as it enters only in the definition of $1/B$).

3. Numerical results

Our simulations were carried out with the ESEL code [21], which numerically solves equations (1)–(4). The dissipative coefficients and the parallel loss times are kept constant in time and space and they are calculated at the inner boundary of the numerical box (but using the SOL connection length, typically evaluated with equilibrium codes). The numerical domain spans $150\rho_s$ in the x direction and $100\rho_s$ in the y direction (i.e. $L_x = 150$ and $L_y = 100$ in normalized units) and it is resolved with 512×256 points. Radially, the first $50\rho_s$ simulate the edge region (i.e. the plasma inside the last closed flux surface), while the remaining $100\rho_s$ describe the SOL. In TCV the last $50\rho_s$ represent the wall shadow, where the parallel connection length is significantly reduced and the Σ parameters are much larger (by a factor of 20 in our simulations). In the MAST simulations no wall shadow is present since the vacuum vessel of this machine has an open configuration and the first wall

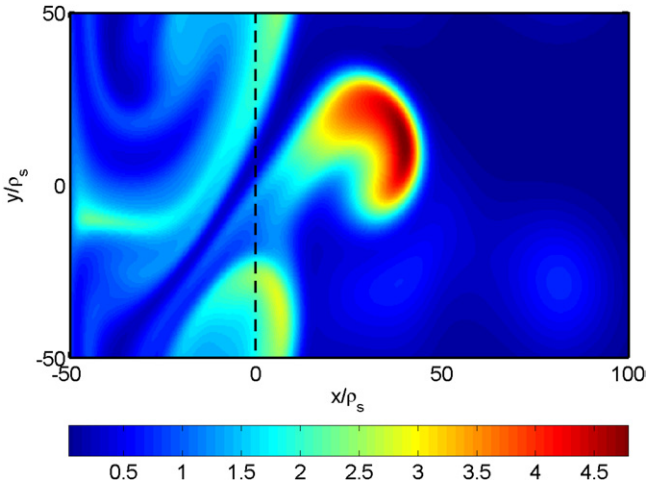

Figure 1. Spatial structure of the density during a blob ejection. The ratio $n(x, y, t = t_0)/\langle n\rangle(x)$ is displayed, where $n(x, y, t = t_0)$ is the density field at the time t_0 and $\langle n\rangle(x)$ is the time and poloidally averaged density profile.

very far from the last closed flux surface. From the numerical point of view, we verified that the choice of a non-equispaced grid did not affect our calculations. Similarly, with specifically devoted simulations, we made sure that a change in the box size or in the resolution did not produce significantly different results.

The scalar quantities are kept constant at the inner boundary of the numerical box, so that $T = T_0$ and $n = n_0$ are fixed and $\Omega = \phi = 0$. At the outer boundary, $\Omega = v_y = 0$ is assumed and zero temperature and density gradients, $\partial T/\partial x = \partial n/\partial x = 0$. Finally, periodicity is imposed in the 'poloidal' direction.

All the simulations are run well beyond the phase in which the turbulence reaches a statistical steady state, typically with strong turbulence in the edge region and with blobs propagating ballistically in the SOL region. The end time is typically of the order of a few tens of msec for MAST, which corresponds to several thousands of turbulence correlation times. Similarly, the cross section of the coherent turbulent structures is of the order of a few tens of ρ_s, much smaller than the box size.

A typical output of the code, which captures a blob ejection during the phase of statistically saturated turbulence, is shown in figure 1. In particular, the ratio between the instantaneous density field and the averaged (in time and poloidal direction) density field, $n(x, y, t = t_0)/\langle n\rangle(x)$, is displayed.

3.1. TCV and MAST

In our first set of simulations, we compared a standard tokamak, TCV, with MAST, which is a spherical tokamak. Despite their different inverse aspect ratio (0.28 for TCV and 0.69 for MAST), both machines share a very similar major radius (0.89 m for TCV and 0.85 m for MAST). TCV data were used in previous works to validate ESEL, with excellent results [17, 18, 23, 24]. On a much smaller scale, ESEL was also used to interpret ion saturation current measurements from the MAST reciprocating probe [34]. Although these were preliminary results, the agreement was good. A companion

Table 1. Typical L-mode plasma and geometrical parameters for TCV and MAST (n_0 and T_0 taken at the last closed flux surface).

	n_0 (10^{19} m^{-3})	T_0 (eV)	B_0 (T)	q	$L_\parallel$ (m)	ϵ	R_0 (m)
TCV	2	20	1.4	3	10	0.28	0.89
MAST	0.8	40	0.5	7	10	0.69	0.85

Table 2. Typical dimensionless parameters for TCV and MAST, corresponding to the dimensional values in table 1. For comparison, in dimensional values the collisional particle diffusion correspond to $D_{\rm TCV} \approx 0.012$ m^2 s^{-1} and $D_{\rm MAST} \approx 0.15$ m^2 s^{-1}.

	D	Σ_n	$\Sigma_{\rm T}$	ρ_s/R
TCV	4.7×10^{-3}	3.3×10^{-5}	1.7×10^{-4}	5.2×10^{-4}
MAST	1.95×10^{-3}	1.25×10^{-4}	3.15×10^{-3}	2.14×10^{-3}

paper [35], to be published in the near future, will be devoted to a thorough comparison between MAST data and ESEL simulations. We anticipate here that we found excellent agreement between the average profiles and the statistics of the ion saturation current measured in MAST discharges and simulated with the ESEL model. This provides an *a posteriori* justification of the model employed in this work which seems to properly capture the relevant physics despite its limitations (i.e. an approximated treatment of the curvature terms and the lack of ion physics which would lead to finite Larmor radius effects).

The typical geometrical and edge parameters for the two machines are given in table 1 and are used to calculate the dimensionless parameters, which are given in table 2. Note that for TCV we have used the same dimensionless parameters as in [23] (including the artificial enhancement of D explained in the reference) and obtained similar results.

We start by examining the average density, $\langle n\rangle$, and temperature, $\langle T\rangle$, profiles. It is useful to clarify that the averages are performed over both time (during the period of statistically saturated turbulence) and 'poloidal' direction, so that a single profile is representative of a whole simulation. Figures 2(*a*) and (*b*) show a comparison of such profiles for MAST and TCV (the curves are normalized to the value of the density or temperature at the inner boundary). In order to highlight the most relevant features of these profiles, we plot also the density and temperature e-folding (or decay) length, defined as $\lambda_n = -\langle n\rangle/(\partial\langle n\rangle/\partial x)$ and $\lambda_T = -\langle T\rangle/(\partial\langle T\rangle/\partial x)$. These quantities, shown in figures 2(*c*) and (*d*), express the typical length over which the particle and heat decay, and therefore give a measure of the width and the steepness of the SOL.

Note that all the averaged profiles are plotted against a normalized radial coordinate, ρ, such that $\rho = -1$ at the inner radial boundary (i.e. $50\rho_s$ inside the last closed flux surface), $\rho = 0$ at the separatrix and $\rho = 2$ at the outer radial boundary (i.e. $100\rho_s$ outside the last closed flux surface). In the TCV simulations, $\rho = 1$ corresponds to the beginning of the wall shadow region while in the MAST simulations it does not bear any specific meaning due to the lack of the wall shadow. All the figures presented in this paper zoom on the region between $-0.25 \leqslant \rho \leqslant 1.25$ in order to focus on the most interesting

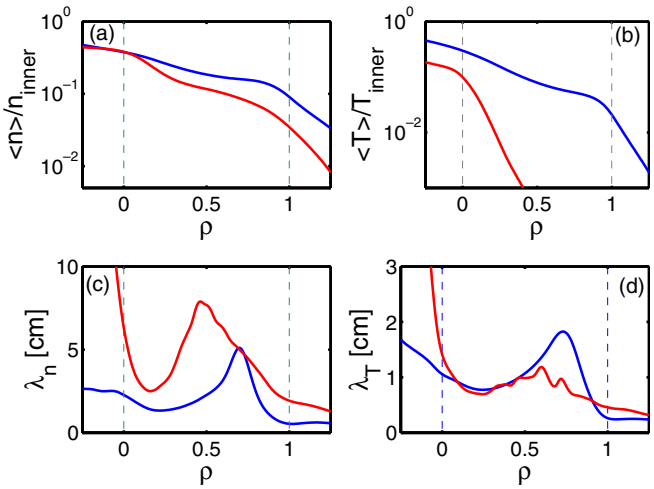

Figure 2. Average density (a) and temperature (b) radial profiles normalized to the value at the inner boundary. Density (c) and (d) temperature e-folding lengths associated. The blue and red lines represent the TCV and MAST case, respectively.

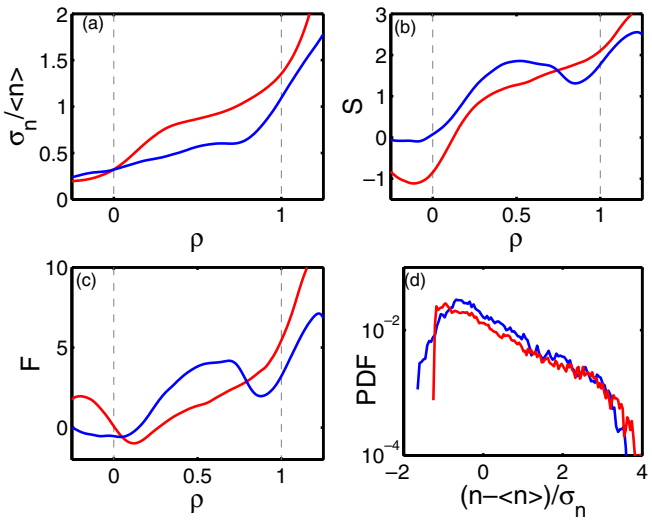

Figure 3. Amplitude of the density fluctuation (a) represented as standard deviation normalized to the average density. The skewness, S, and the flatness, F, of the PDF are shown in (b) and (c). The PDF of the density fluctuations evaluated at $\rho = 0.4$ is shown in (d). The blue and red lines represent the TCV and MAST case, respectively.

part of the SOL. Furthermore, temperature profiles under a few eV would not be physical as the model used in our calculations would lose its validity, and are therefore not shown.

It is interesting to note that despite the two machines being dimensionally similar (as far as the major radius is concerned) and operate at comparable plasma temperature and density, the density SOL width is twice as large in MAST compared with TCV (1.3 cm for TCV and 2.5 for MAST). We evaluate such a width by comparing the minimum of λ_n in the near SOL. On the other hand, the temperature width is similar for both machines and slightly below 1 cm. In the far SOL ($\rho > 1$) the density and temperature in TCV decrease more rapidly as a consequence of the higher parallel losses due in the wall shadow (this is especially true for $\rho > 1.2$, not shown in the figure). This effect is not present in the MAST profiles.

As TCV and MAST are operating in completely different regimes (i.e. all the dimensionless parameters significantly change), the interpretation of these results is not straightforward. This suggests an approach aimed at disentangling the complexity of the problem. This is what we will do in the next subsections, where the decay lengths in the SOL are systematically studied by varying the edge variables, one at a time. The purpose of this subsection is only to compare a standard tokamak with a spherical tokamak, leaving the detailed interpretation of the results to the next subsections (in particular sections 3.4 and 3.7).

We pass now to the discussion of the turbulence statistics. Judging from table 2, the turbulence drive, ρ_s/R, is four times larger in MAST than in TCV. Since the major radius is virtually identical for the two machines, this is due to the fact that in the spherical tokamak the hybrid Larmor radius is four times larger than in TCV (the temperature is higher and the magnetic field is lower in MAST). This results in larger fluctuations in MAST. Figure 3(a) shows the standard deviation of the density fluctuations, σ_n, divided by the average density as a function of the radial variable. In the SOL region this quantity is larger for MAST than for TCV, especially beyond $\rho = 1$, where the wall shadow quenches the TCV blobs (not shown).

Figures 3(b) and (c) depict a similar non-Gaussian behaviour in both machines. In particular, figures 3(b) and (c) show the skewness, S, and the flatness (or excess kurtosis), F, of the probability distribution function (PDF) of the density signal, both of which are zero for a Gaussian distribution. A negative value of the skewness is indicative of a predominance of negative bursts in the time series of the signal, while a positive value is associated with the opposite behaviour. We then see from figure 3(b) that plasma holes (i.e. lower density than average) are present in the region inside the last closed flux surface, where $S < 0$, and plasma blobs (i.e. density higher than average) erupt in the SOL region. The flatness of the signal, in figure 3(c), represents the peakedness of the PDF. The higher F, the more bursty events are present in a certain location. Finally, for completeness, we show in figure 3(d) the PDF of the density fluctuations at the radial location $\rho = 0.4$.

3.2. *Edge temperature scan*

While the inter-machine comparison of the SOL behaviour described above is useful to appreciate the differences between a standard and a spherical tokamak, it does not provide a systematic understanding of the SOL response to external changes. In this subsection we describe an edge temperature scan in a MAST relevant configuration. The most obvious, but not unique, way to affect the edge temperature is to modify the input power. However, variations in other engineering quantities can have a similar effect. For example, increasing the line-averaged density through plasma fuelling typically decreases the edge temperature (see the discussion in subsection 3.4).

In our scan, all the relevant quantities are kept constant and equal to those shown in table 1, apart form the temperature, which is reduced from 40 to 20 eV in steps of 10 eV. Independent simulations were carried out for each value of the temperature.

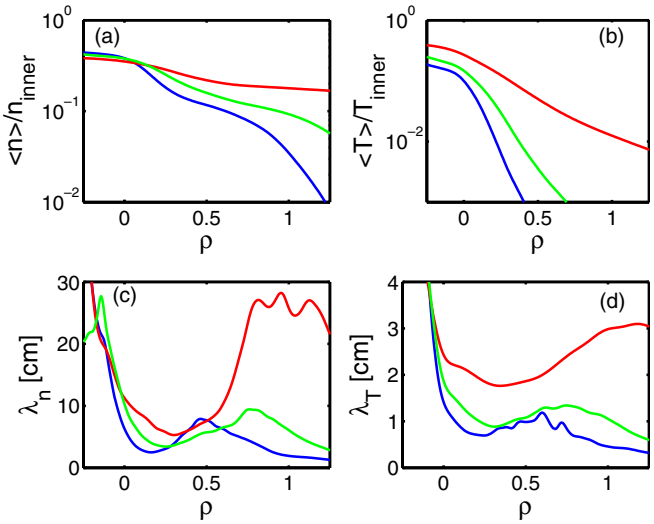

Figure 4. Average density (a) and temperature (b) radial profiles normalized to the value at the inner boundary. Density (c) and (d) temperature e-folding lengths associated. The blue, green and red lines represent $T = 40$ eV, $T = 30$ eV and $T = 20$ eV, respectively.

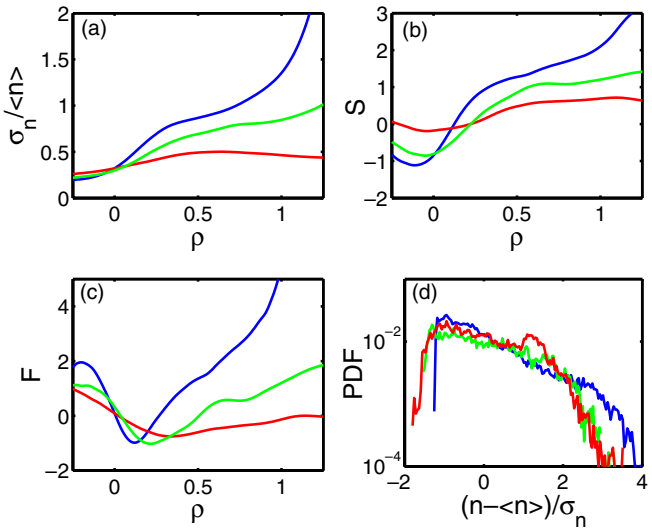

Figure 5. Amplitude of the density fluctuation (a) represented as standard deviation normalized to the average density. The skewness, S, and the flatness, F, of the PDF are shown in (b) and (c). The PDF of the density fluctuations evaluated at $\rho = 0.4$ is shown in (d). The blue, green and red lines represent $T = 40$ eV, $T = 30$ eV and $T = 20$ eV, respectively.

The average density and temperature profiles resulting from these simulations are shown in figures 4(a) and (b). Similarly to what we did in the previous subsection, also the density and temperature e-folding lengths are evaluated and shown in figures 4(c) and (d). It is evident that an edge temperature strongly affects the average profiles, with narrower SOL width at higher temperatures. For example, at 20 eV the temperature and, more markedly, the density profiles are particularly flat as a result of the fact that the parallel losses are weaker than at 40 eV (hence the filaments are dissipated less efficiently and propagate their density and temperature excess further out). In this regime, the width of the SOL shows a rough linear scaling with the inverse of the temperature, so that at 20 eV the density width of the SOL is around 5.2 cm.

Also the fluctuating quantities show a dependence on the edge temperature, although less marked. A first, simple explanation for this behaviour is that the interchange drive decreases with the temperature, thus leading to a less violent turbulence. In addition, a lower temperature is associated with larger collisional dissipative parameters, which have a quenching effect on the fluctuations. The result is that lower temperatures are associated with smaller relative fluctuations (see figure 5(a)) and a less intermittent behaviour reflected by a statistics with fewer extreme events (see figures 5(b), (c) and (d)).

3.3. Edge density scan

The main aim of the edge density scan is to understand the SOL response for different levels of fuelling. We carried out three simulations with densities 0.8×10^{19}, 1.2×10^{19} and 1.4×10^{19} m^{-3}, while all the other plasma and geometrical parameters were kept equal to those in table 1.

The variation of the density is therefore rather significant, considering that it changes by almost a factor 2. Despite

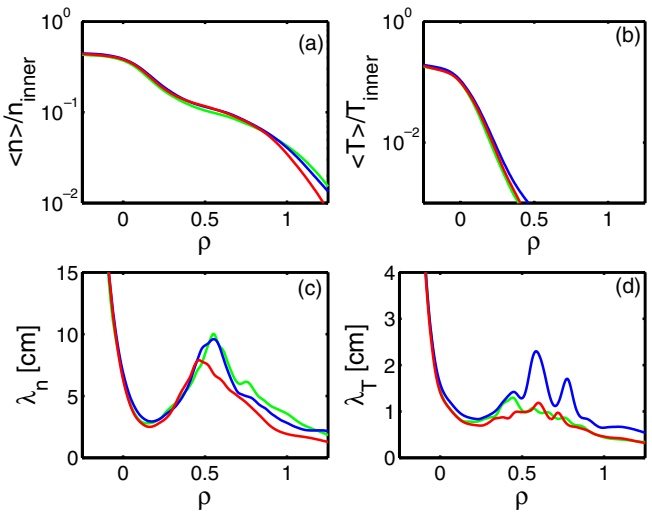

Figure 6. Average density (a) and temperature (b) radial profiles normalized to the value at the inner boundary. Density (c) and (d) temperature e-folding lengths associated. The blue, green and red lines represent 0.8×10^{19} m^{-3}, 1.2×10^{19} m^{-3} and 1.4×10^{19} m^{-3}, respectively.

that, the response of the SOL is negligible, so that both the profiles and the fluctuating quantities remain almost unchanged. Figures 6(a) and (b) show remarkably similar density and temperature profiles, especially in the edge and near SOL region. This similarity persists when we compare the SOL width, see figures 6(c) and (d).

Also the statistics of the turbulence are independent of the density variations. In particular, the skewness and flatness of the density PDF, figures 7(b) and (c), show the same radial trend and comparable magnitude. Similarly, the amplitude of the fluctuations is very similar in all three cases in the region $\rho < 1$.

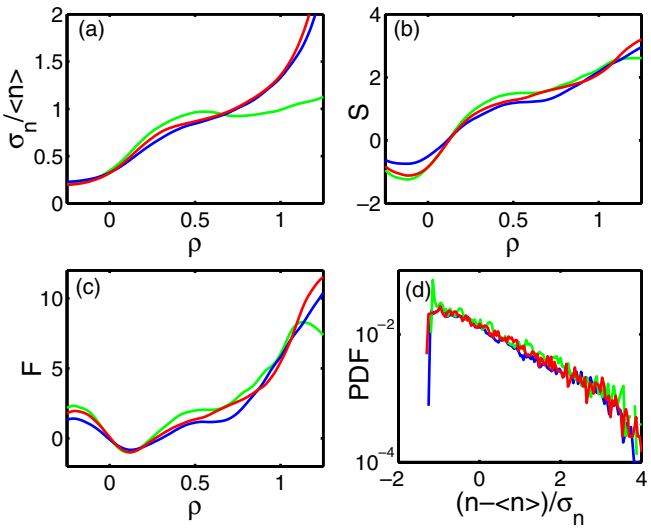

Figure 7. Amplitude of the density fluctuation (a) represented as standard deviation normalized to the average density. The skewness, S, and the flatness, F, of the PDF are shown in (b) and (c). The PDF of the density fluctuations evaluated at $\rho = 0.4$ is shown in (d). The blue, green and red lines represent 0.8×10^{19} m^{-3}, 1.2×10^{19} m^{-3} and 1.4×10^{19} m^{-3}, respectively.

3.4. Interpretation of the edge temperature and density scans

The result of the previous two subsections can be interpreted by looking at the effect of the edge temperature and density on the dimensionless parameters governing the problem and by explaining how such changes modify the dynamics of the blobs in the SOL (which eventually determine the profiles and the fluctuation statistics).

First of all, note that the temperature affects all the plasma dimensionless parameters (see equations (10)–(13)) and it can be therefore expected to play a major role in the dynamics of the filaments. On the other hand, the density mainly affects the dissipative parameters D, χ and μ, while it does not modify the particle and momentum parallel losses or the interchange drive. In addition, the dependence of the perpendicular dissipative parameters on the density is weaker than on the temperature (the exponent of the former is 1, while for the latter is 3/2). The temperature parallel loss term depends on the density through the electron collisionality, but this is a weak effect in the regime we are investigating.

Our edge temperature and density scans seem to suggest that, for the cases studied, a variation of the dissipative parameters alone (as produced by the density) does not change significantly the nature of the turbulence or the transport it produces. This is consistent with the picture of blobs travelling in the SOL, but produced in the edge. Indeed, once in the SOL the perpendicular diffusion will contribute to spread the coherent structure in the perpendicular plane and reduce the amplitude of the perturbation, but it will not, as a first approximation, affect the distance it travels (which determines the average profiles). Such distance is correlated with the ballistic velocity of the blob which, for filaments detached from the sheath, is proportional to the square root of the perpendicular size of the coherent structure and to the square root of the relative amplitude of the thermodynamic variable (i.e. temperature or density) with respect to the background [22, 36]. The two effects are therefore likely to cancel out, leaving the ballistic velocity (and hence the penetration distance for identical parallel losses) roughly unaltered.

On the other hand, the parallel losses (and hence the edge temperature) seem to have a much more significant effect on the penetration of the blobs. The Σ terms contribute to reduce the amplitude as well as the size of the perturbations, thus dissipating the blobs as they proceed towards the wall. As suggested in section 3.2, a blob unhindered by significant parallel losses can travel further out and carry its full load of excess density and particles deeper in the SOL, thus leading to flatter average profiles.

It is important, at this point, to relate our results and our interpretations to experimental observations. Several papers have described how the fuelling and a varying line-averaged density, $\overline{n}$, affect the SOL characteristics [4, 5, 7, 10–12, 14, 15, 17, 37].

These works agree on the fact that a larger line-averaged density induces flatter and broader profiles in the SOL. This, at first sight, seems in contradiction with the results of section 3.3. However, the disagreement is only apparent. Indeed, as the line-averaged density is modified by increasing the fuelling, both the edge density *and* temperature change (the former increases and the latter decreases). As a consequence, a scan in $\overline{n}$ is not a good proxy for a scan in n_0, since also T_0 changes at the same time. This effect was observed in both tokamaks [5, 7, 14] and spherical tokamaks (MAST) [26, 27] but it was usually disregarded as the edge temperature change is moderate at best (around a factor two). However, as shown in section 3.2, the SOL seems extremely sensitive to variations of T_0.

Thus, our interpretation is that larger line-averaged densities lead to broader profiles as a consequence of the drop in the edge temperature rather than the increase in the edge density. Convincing evidence of this mechanism can be found in [5, 12]. In particular, figure 9 in [5] shows profile broadening in a case in which n_0 is basically constant and T_0 decreases by a factor three. Symmetrically, figures 5(a) and (b) in [12] show very little broadening when T_0 is held fixed in a line-averaged density scan. These experimental observations are therefore in qualitative agreement with our results in sections 3.2 and 3.3.

Finally, it is useful to remark that the mechanism for the profile broadening in line-averaged density scans proposed in this section is complementary, not alternative to previous interpretations. In particular, in [17] the flattening of the SOL profiles was associated with the transition from sheath to conduction limited regime for the plasma filament, which occurs at small collisionality. In the sheath-limited regime (valid for small edge density) the parallel losses are more important (because of the sheath currents) and therefore the blob penetration in the SOL smaller [22]. As the edge density and the collisionality increase the parallel losses reduce and the profile broadens. Our simulations cannot capture this effect as our model is valid only for conduction limited regimes. However, within such a regime (typical in most tokamaks), our interpretation holds.

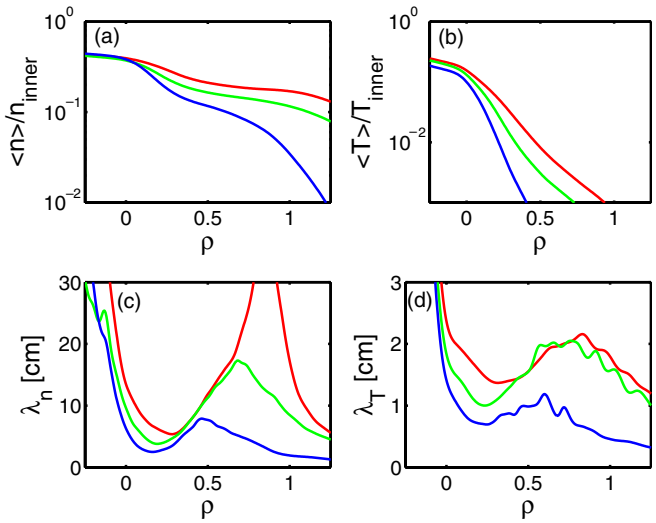

Figure 8. Average density (a) and temperature (b) radial profiles normalized to the value at the inner boundary. Density (c) and (d) temperature e-folding lengths associated. The blue, green and red lines represent $q = 7$ and $L_\parallel = 10\,\mathrm{m}$, $q = 8.7$ and $L_\parallel = 12\,\mathrm{m}$ and $q = 10$ and $L_\parallel = 14\,\mathrm{m}$, respectively. Larger q and $L_\parallel$ represent smaller total currents.

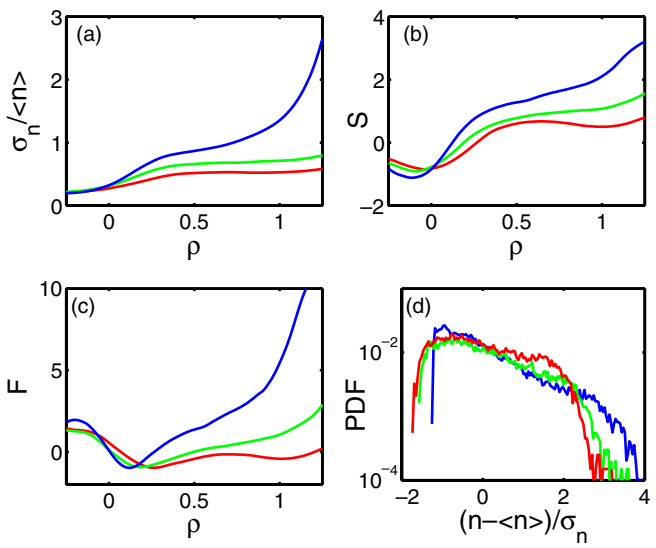

Figure 9. Amplitude of the density fluctuation (a) represented as standard deviation normalized to the average density. The skewness, S, and the flatness, F, of the PDF are shown in (b) and (c). The PDF of the density fluctuations evaluated at $\rho = 0.4$ is shown in (d). The blue, green and red lines represent $q = 7$ and $L_\parallel = 10\,\mathrm{m}$, $q = 8.7$ and $L_\parallel = 12\,\mathrm{m}$ and $q = 10$ and $L_\parallel = 14\,\mathrm{m}$, respectively. Larger q and $L_\parallel$ represent smaller total currents.

3.5. Current scan

At fixed toroidal magnetic field, changing the plasma current affects both q and $L_\parallel$. In order to reproduce the effects of a current scan we run three simulations with ($q = 7$; $L_\parallel = 10\,\mathrm{m}$), ($q = 8.7$; $L_\parallel = 12\,\mathrm{m}$) and ($q = 10$; $L_\parallel = 14\,\mathrm{m}$) and all the other parameters as in table 1. The choice of the parallel connection length in the new cases was determined by maintaining the ratio $L_\parallel/q$ constant (in order to satisfy the approximate relation $L_\parallel \sim qR$). It is useful to recall that the edge safety factor is inversely proportional to the total toroidal current flowing in the plasma, $q \sim I^{-1}$, so that a decreasing q represents an increasing I. Note that our current scan is not equivalent to a scan in B_0, which would similarly lead to a change in q and $L_\parallel$ but would also directly affect the dimensionless parameters (see equations (10)–(13)).

Our simulations show a clear broadening of the density and temperature-averaged profiles as the current is decreased, figures 8(a) and (b). This is confirmed by the calculation of the e-folding length, shown in figures 8(c) and (d). Also the fluctuation statistics show a weak but visible dependence on I. In particular, stronger currents are associated with larger fluctuation amplitudes, skewness and flatness, and hence with a more bursty behaviour, see figure 9.

The numerical results presented in this subsection are compatible with experimental observations. In particular, in DIII-D [13] and TCV [18] broader SOL profiles were reported for small plasma current and [18] also showed a weak dependence for the amplitude of the density fluctuations (skewness and flatness are more difficult to interpret as the experimental data are rather scattered). In addition, [37] has reported an increase in λ_n and λ_T with q on several machines, which is again compatible with our results. Similarly, [38] gives a λ_n and λ_T dependence on q that is slightly larger than linear for JET plasmas. As described in figure 10, our

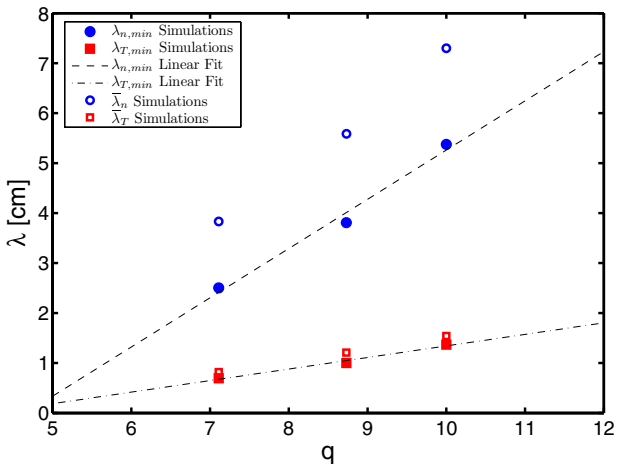

Figure 10. Typical density and temperature decay lengths as a function of the edge safety factor. The full symbols represent $\lambda_{n,\mathrm{min}}$ ($\lambda_{T,\mathrm{min}}$), which is the minimum of λ_n (λ_T) in the near SOL (see figure 8). The lines show the linear interpolation of these numerical points. The open symbols represent $\bar{\lambda}_n$ (circles) and $\bar{\lambda}_T$ (squares), see definition in the text.

numerical results show an inverse dependence of the decay lengths with the plasma current (or linear in q). In this figure the characteristic decay lengths are represented by the minimum value of λ_n (full circles) and λ_T (full squares) in the near SOL and also by an 'averaged' value (open symbols) which encompasses the region $0 \leqslant \rho \leqslant 0.5$, $\bar{\lambda}_n \equiv -0.5/\log[n(\rho = 0)/n(\rho = 0.5)]$ (replacing n with T in the previous expression gives $\bar{\lambda}_T$).

3.6. Effect of the parallel connection length

In this subsection, we discuss the effect of a longer divertor leg on the features of the SOL. As before, our assumption is

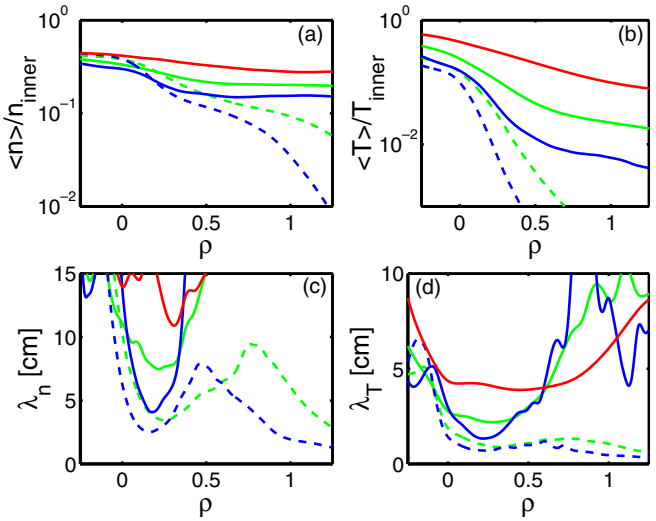

Figure 11. Average density (*a*) and temperature (*b*) radial profiles normalized to the value at the inner boundary. Density (*c*) and (*d*) temperature e-folding lengths associated. The blue, green and red lines represent $T = 40$ eV, $T = 30$ eV and $T = 20$ eV, respectively, for a connection length $L_\parallel = 20$ m. The blue and green dashed lines represent $T = 40$, $T = 30$ eV for a connection length $L_\parallel = 10$ m and are added to simplify the comparison between the two cases (high and low $L_\parallel$).

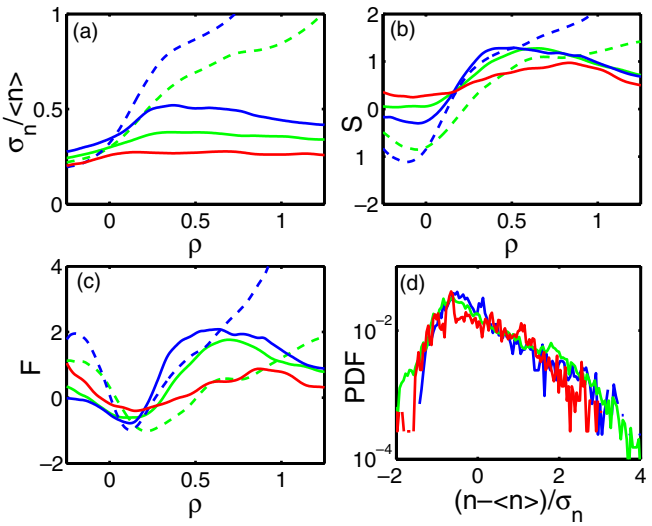

Figure 12. Amplitude of the density fluctuation (*a*) represented as standard deviation normalized to the average density. The skewness, S, and the flatness, F, of the PDF are shown in (*b*) and (*c*). The blue, green and red lines represent $T = 40$ eV, $T = 30$ eV and $T = 20$ eV, respectively for a connection length $L_\parallel = 20$ m. The PDF of the density fluctuations evaluated at $\rho = 0.4$ is shown in (*d*). The blue and green dashed lines represent $T = 40$ eV, $T = 30$ eV for a connection length $L_\parallel = 10$ m and are added to simplify the comparison between the two cases (high and low $L_\parallel$).

that all other parameters (including the safety factor) remain the same. Within the same machine, this effect can be achieved by shifting the plasma using the control coils, but this change is only modest. More radically, one can think of varying the mid-plane to target parallel connection length by changing the configuration of the machine, for example by replacing the divertor. The Super-X divertor that will be installed on the upgraded version of MAST is an attempt in this direction.

It is appropriate to mention that a new divertor is likely to affect also the upstream plasma parameters such as the operating density and the temperature, so that the length of the divertor leg will not be the only quantity that will change. However, a complete discussion of the physics involved would require an integrated modelling effort, which should include a study of the perpendicular as well as the parallel transport in the SOL together with an adequate modelling of the core response. This is beyond the purpose of the work presented here, which can anyway give indications on how the main players (edge temperature, edge density and parallel connection length) act on the SOL *independently*.

In order to assess the effect of the parallel connection length we have repeated the temperature scan of section 3.2 with $L_\parallel$ twice as long (i.e. $L_\parallel = 20$ m). Our results are shown in figures 11 and 12 for the average profiles and turbulence statistics. The main message of these figures is that the longer parallel connection length makes the profiles flatter and the density PDF less characterized by extreme events.

3.7. Interpretation of the current scan and the parallel connection length

With our simulations, we found that decreasing the total plasma current or lengthening the divertor leg broadens the SOL profiles and makes the turbulence less intermittent (although this is a weaker effect). This is similar to the effect obtained when the edge temperature is reduced.

This is hardly surprising if we compare where T_0, q and $L_\parallel$ appear in the definitions of the dimensionless parameters, see equations (10)–(13). A longer $L_\parallel$ makes the parallel loss terms smaller, which allows a deeper penetration in the SOL of the turbulent structures expelled by the core plasma. The same result can be achieved by reducing the edge temperature (see section 3.2).

On the other hand, the parallel connection length does not affect the dissipative parameters, while q and T_0 (as well as n_0) do. However, it seems like the dissipative parameters do not play an important role in determining the profiles or the fluctuations in the regimes we are considering. As a test, we evaluated the effect of a change in the perpendicular dissipation (D, χ and μ) while keeping the other dimensionless parameters unaltered. This was carried out by repeating the simulations of section 3.5 while keeping $L_\parallel$ fixed at the value of 10 m (i.e. we did a pure q scan). What we found were negligible changes to all the SOL features (not shown in this paper). This, together with the results of section 3.3 leads us to the conclusion that, in the regime investigated, the width of the SOL is mainly determined by the parallel loss terms.

Finally, the interchange drive is reduced by a smaller edge temperature, while the parallel connection length or the safety factor does not affect it. Hence, while the overall effect of increasing $L_\parallel$ or reducing the total current is similar to decreasing T_0, the three mechanisms are not exactly identical.

4. Summary and conclusions

We have carried out a numerical study of the sensitivity of the turbulence in the scrape-off-layer to the variation of different edge physical quantities. In particular, we have focused on a plasma regime relevant for L-mode plasmas in MAST. Scans in the typical edge temperature, density and current were performed and used to interpret the effect of changes in input power and fuelling on the SOL. In addition, we studied the effect of a longer mid-plane to target connection length, with the aim of understanding the operating configuration of the new Super-X divertor that will be installed on MAST.

Our model is well suited to describe interchange turbulence, and particularly focuses on the evolution of the blobs once they detach from the last closed flux surface. Indeed, the L-mode edge turbulence is more likely to be caused by highly non-linear electromagnetic drift-wave turbulence [32], which cannot be represented within our model. However, replacing the 'turbulence engine' (from drift-wave to interchange driven) in the edge region should have little effect on the evolution of the filamentary structures in the SOL region (the region of plasma we want to describe), where the interchange mechanism dominates [30, 39].

Our simulations provide a broad overview of the turbulent dynamics and the SOL features in the parameter space relevant for the MAST experiment. The temperature scan showed that the SOL width, associated with the e-folding length of the density and temperature profiles, increases as the edge temperature decreases. At the same time, the density PDF becomes less skewed and more peaked, so that it represents a less bursty and more 'Gaussian' statistic (although the effect on the fluctuation statistics is less dramatic than the effect on the averaged profiles). A realistic edge density variation, on the other hand, does not affect the SOL as neither the shape of the average (in time and 'poloidal' direction) profiles nor the dynamics of the turbulence show significant changes. In addition, an increase of the parallel connection length has a similar, but not identical, effect to reducing the edge temperature. Our simulations were also able to correctly reproduce the inverse dependence of the decay length on the plasma current. In addition, we find a certain degree of universality in the turbulence [10, 17], the statistics of which do not significantly change in our scans. Our numerical results are in qualitative agreement with experimental observations and help one to single out the contribution of each physical quantity to the dynamics of the SOL.

All these effects can be interpreted using the dimensionless parameters that govern the dynamics of the system, equations (10)–(13). In particular, we observe that a realistic variation of the perpendicular dissipative parameters does not significantly affect the problem in the regimes we have investigated. On the other hand, the parallel loss terms play a crucial role in determining the width of the SOL as they contribute to hinder the propagation and quench the amplitude of the plasma blobs expelled from the last closed flux surface.

Acknowledgments

FM acknowledges useful discussions with Dr A Kirk, Dr J Harrison and Dr G Fishpool. This work was funded by the RCUK Energy Programme under grant EP/I501045 and the European Communities under the contract of Association between EURATOM and CCFE. The views and opinions expressed herein do not necessarily reflect those of the European Commission.

Euratom © 2012.

References

[1] Loarte A *et al* 2007 *Nucl. Fusion* **47** S203
[2] Zweben S J and Gould R W 1985 *Nucl. Fusion* **25** 171
[3] Wootton A J *et al* 1990 *Phys. Fluids* B **2** 2879
[4] LaBombard B *et al* 2000 *Nucl. Fusion* **40** 2041
[5] LaBombard B *et al* 2001 *Phys. Plasmas* **8** 2107
[6] Boedo J A *et al* 2001 *Phys. Plasmas* **8** 4826
[7] Lipshultz B, LaBombard B, Pitcher C S and Bovin R L 2002 *Plasma Phys. Control. Fusion* **44** 733
[8] Boedo J A *et al* 2003 *Phys. Plasmas* **10** 1670
[9] Zweben S J *et al* 2004 *Nucl. Fusion* **44** 134
[10] Graves J P, Horacek J, Pitts R A and Hopcraft K I 2005 *Plasma Phys. Control. Fusion* **47** L1
[11] Lipshultz B, Whyte D G and LaBombard B 2005 *Plasma Phys. Control. Fusion* **47** 1559
[12] Whyte D G *et al* 2005 *Plasma Phys. Control. Fusion* **47** 1579
[13] Rudakov D L 2005 *et al Nucl. Fusion* **45** 1589
[14] LaBombard B *et al* 2005 *Nucl. Fusion* **45** 1658
[15] Horacek J *et al* 2005 *Czech. J. Phys.* **55** 271
[16] Dudson B D, Dendy R O, Kirk A, Meyer H and Counsell G F 2005 *Plasma Phys. Control. Fusion* **47** 885
[17] Garcia O E *et al* 2007 *Nucl. Fusion* **47** 667
[18] Garcia O E *et al* 2007 *Plasma Phys. Control. Fusion* **49** B47
[19] Sarazin Y and Ghendrih Ph 1998 *Phys. Plasmas* **5** 4214
[20] Krashenninikov S I 2001 *Phys. Lett.* A **283** 368
[21] Garcia O E, Naulin V, Nielsen A H and Rasmussen J J 2004 *Phys. Rev. Lett.* **92** 165003
[22] Garcia O E, Bian N H and Fundamenski W 2006 *Phys. Plasmas* **13** 082309
[23] Garcia O E *et al* 2006 *Plasma Phys. Control. Fusion* **48** L1
[24] Garcia O E *et al* 2007 *J. Nucl. Mater.* **363–365** 575
[25] Fundamenski W *et al* 2007 *Nucl. Fusion* **47** 417
[26] Harrison J 2012 Private communication
[27] Elmore S *et al* 2012 *Plasma Phys. Control. Fusion* **54** 065001
[28] Kirk A *et al* 2004 *Phys. Rev. Lett.* **92** 245002-1
[29] Kirk A *et al* 2006 *Plasma Phys. Control. Fusion* **48** B433
[30] Dudson B D *et al* 2008 *Plasma Phys. Control. Fusion* **50** 124012
[31] Valanju P M, Kotschenreuther M, Mahajan S M and Canik J 2009 *Phys. Plasmas* **16** 056110
[32] Scott B 1997 *Plasma Phys. Control. Fusion* **39** 1635
[33] Militello F and Fundamenski W 2011 *Plasma Phys. Control. Fusion* **53** 095002
[34] Tallents S 2009 *PhD Thesis* Imperial College London
[35] Militello F *et al* 2012 *Plasma Phys. Control. Fusion* submitted
[36] Garcia O E, Bian N H, Naulin V, Nielsen A H and Rasmussen J J 2005 *Phys. Plasmas* **12** 090701
[37] ITER Physics Expert Group on Divertor *et al* 1999 *Nucl. Fusion* **39** 2391
[38] Fundamenski W 2008 *Fusion Sci. Technol.* **53** 1023
[39] Ribeiro T T and Scott B 2005 *Plasma Phys. Control. Fusion* **47** 1657